Modeling Extreme Mass Ratio Inspirals within the Effective-One-Body Approach

Nicolás Yunes,[1] Alessandra Buonanno,[2] Scott A. Hughes,[3] M. Coleman Miller,[4] and Yi Pan[2]

[1]*Department of Physics, Princeton University, Princeton, NJ 08544, USA.*
[2]*Maryland Center for Fundamental Physics, Department of Physics, University of Maryland, College Park, MD 20742, USA.*
[3]*Department of Physics and MIT Kavli Institute, 77 Massachusetts Avenue, Cambridge, MA 02139, USA.*
[4]*Maryland Astronomy Center for Theory and Computation, Department of Astronomy, University of Maryland, College Park, MD 20742, USA.*

We present the first models of extreme-mass-ratio inspirals within the effective-one-body (EOB) formalism, focusing on quasi-circular orbits into non-rotating black holes. We show that the phase difference and (Newtonian normalized) amplitude difference between analytical EOB and numerical Teukolsky-based gravitational waveforms can be reduced to $\lesssim 10^{-1}$ rads and $\lesssim 2\times10^{-3}$, respectively, after a 2-year evolution. The inclusion of post-Newtonian self-force terms in the EOB approach leads to a phase disagreement of $\sim$ 6–27 rads after a 2-year evolution. Such inclusion could also allow for the EOB modeling of waveforms from intermediate-mass ratio, quasi-circular inspirals.

Introduction. Extreme mass ratio inspirals (EMRIs) are the gravitational wave (GW) driven coalescences of stellar mass compact objects with supermassive black holes (SMBHs). When the large black hole's (BH's) mass is in the range $10^5\,M_\odot - 10^7\,M_\odot$, EMRI waves are emitted at frequencies well suited to measurement by the planned *Laser Interferometer Space Antenna* (LISA). Because EMRI events are expected to be abundant [1] and will carry detailed information about strong-field spacetimes near SMBHs [2], they are high-priority targets for LISA observation. The intrinsic feebleness of these waves will require accurate waveform templates to detect and faithfully measure the signals produced by Nature. Because EMRIs can spend thousands of cycles in the close vicinity of the SMBH's innermost stable circular orbit (ISCO), traditional post-Newtonian expansions are not well suited to modeling their signals; the binary's orbital speed is $v/c \sim 0.1$–0.5, a regime where traditional post-Newtonian techniques perform poorly. Numerical models built using BH perturbation theory should be able to reliably model EMRI signals. However, the computational cost of covering the full span of EMRI parameter space (including effects due to BH spin, non-equatorial orbits, and eccentricity) is likely to be very high [1].

This has motivated us to examine techniques for reliably approximating these waves at a much smaller computational cost. The effective-one-body (EOB) formalism was introduced as a way to analytically describe the inspiral, merger, and ringdown waves emitted by comparable-mass BH binaries [3, 4]. This formalism was then extended to higher post-Newtonian (PN) orders [5], spinning BHs [6–8], small mass-ratio mergers [9, 10], and was further improved by introducing factorized waveforms [10, 11]. By calibrating a few adjustable parameters in the EOB-dynamics and waveforms, [12, 13] showed that the phase and amplitude of the EOB and numerical-relativity waveforms can be made to agree within the numerical error of the simulations, thus providing GW detectors with faithful templates. In this analysis, we consider calibrating EOB with BH perturbation theory templates in order to similarly model EMRI waves. Such an analysis must be done separately from the previous EOB-numerical relativity calibration, because sufficiently long numerical relativity simulations are currently not available for EMRIs. This is because the large mass ratio in EMRI systems leads to tens to hundreds of thousands of detectable cycles within a one-year window using LISA, thus requiring extremely long simulations that are currently computationally prohibitive.

As a first step, we restrict our models to a small compact object spiraling along a quasi-circular orbit into a non-spinning SMBH [14]. Although the assumptions of circularity and zero spin can and will be relaxed in the future, there exist astrophysical motivations for this initial choice of binary configuration. For example, the tidal separation scenario for EMRIs [15] implies nearly circular but arbitrarily inclined orbits in the $> 10^{-4}$ Hz frequency band relevant for LISA, and the accretion disk capture picture [16–18] implies orbits that are both nearly circular and in the equatorial plane of the SMBH. In addition, the characteristics of the SMBHs themselves are uncertain in the $< 10^7\ M_\odot$ mass range most relevant for LISA. In some astrophysical scenarios, the growth of these BHs is dominated by the accretion of stars moving on random trajectories, instead of by the accretion of gas disks, thought to be more important for higher-mass SMBHs [19]. Such growth would lead to $\hat{a} \equiv |\vec{J}|/M^2 \ll 1$ (in natural units with $G = c = 1$, which we use throughout this paper), hence the Schwarzschild (nonrotating) spacetime is a reasonable first approximation.

We now systematically compare EMRI waveforms computed in the EOB approach to those calculated using BH perturbation theory via the numerical solution of the Teukolsky equation [20–23]. As we describe in the remainder of this *Letter*, we find that appropriately cali-

brated EOB waveforms in fact do an excellent job modeling waves computed using BH perturbation theory. This suggests that the EOB scheme is very likely to be an outstanding tool for modeling EMRI waves in future LISA data analysis.

Analytical and Numerical Modeling. For a BH binary with masses m_1 and m_2, we set $M = m_1 + m_2$ and $\mu = m_1 m_2/M = \nu M$. In absence of spins, the motion is constrained to a plane. Let us introduce Schwarzschild-like coordinates (r, Φ) (where r is M-normalized) centered on the binary's center of mass, as well as their reduced (μ-normalized) conjugate momenta (p_r, p_Φ). The non-spinning EOB Hamiltonian then reads [3] $H^{\rm real} = M\sqrt{1 + 2\nu\,[(H^{\rm eff} - \mu)/\mu]} - M$, where the effective Hamiltonian is [3, 5, 10]

$$H^{\rm eff} = \mu \sqrt{p_{r_*}^2 + A(r)\left[1 + \frac{p_\Phi^2}{r^2} + 2(4-3\nu)\,\nu\,\frac{p_{r_*}^4}{r^2}\right]}\,. \quad (1)$$

We use here the reduced conjugate momentum p_{r_*} to the EOB *tortoise* radial coordinate r_* because it improves the numerical stability of the code [10]. The tortoise coordinate is defined via $dr_*/dr = \sqrt{D(r)}/A(r)$, where $A(r)$ and $D(r)$ are obtained by applying the Padé resummation [5] to the Taylor-expanded forms [3, 5]

$$A_{\rm T}(r) \;=\; 1 - \frac{2}{r} + \frac{2\nu}{r^3} + \left(\frac{94}{3} - \frac{41}{32}\pi^2\right)\nu\,\frac{1}{r^4}\,, \quad (2)$$

$$D_{\rm T}(r) \;=\; 1 - \frac{6\nu}{r^2} + 2\nu\,(3\nu - 26)\,\frac{1}{r^3}\,. \quad (3)$$

The EOB Hamilton equations are written in terms of the reduced (dimensionless) quantities $\widehat{H}^{\rm real} \equiv H^{\rm real}/\mu$, $\widehat{t} = t/M$ [4]:

$$\frac{dr}{d\widehat{t}} \;=\; \frac{A(r)}{\sqrt{D(r)}}\frac{\partial \widehat{H}^{\rm real}}{\partial p_{r_*}}\,, \qquad \frac{d\Phi}{d\widehat{t}} = \frac{\partial \widehat{H}^{\rm real}}{\partial p_\Phi}\,, \quad (4)$$

$$\frac{dp_{r_*}}{d\widehat{t}} \;=\; -\frac{A(r)}{\sqrt{D(r)}}\,\frac{\partial \widehat{H}^{\rm real}}{\partial r}\,, \qquad \frac{dp_\Phi}{d\widehat{t}} = \widehat{\mathcal{F}}_\Phi\,, \quad (5)$$

where $\widehat{\mathcal{F}}_\Phi$ is a Padé-resummed radiation-reaction force [4, 24], related to the GW energy dissipation to be defined later. Initial data is obtained through a mock evolution, which is initialized at an initial orbital separation of $100M$ using initial conditions for a quasi-circular inspiral [4].

With the EOB inspiral dynamics in hand, we compute the multipole-decomposed GW $h_{\ell m}$ (ℓ and m refer to spherical harmonics), following the factorized PN prescription of [11], which depends directly on orbital quantities. The EOB GW phase is computed by solving $\dot{\Phi}_{\ell m} = -(1/m)\,{\rm Im}[\dot{h}_{\ell m}/h_{\ell m}]$. Errors in the EOB waveforms arise due to inaccuracies in the numerical solution of Eqs. (4) and (5) and inaccurate initial data. We have investigated such sources of error and estimate them to be no worse than $\delta\Phi_{22} \lesssim 0.03$ rads in the waveform's phase and $\delta h_{22}/h_{22} \lesssim 10^{-7}$ in the normalized amplitude after a 2-year evolution. This cumulative error is primarily dominated by the accuracy of the routine used in `Mathematica` to solve Eqs. (4) and (5).

We compare EOB waves with waveforms computed in BH perturbation theory by solving the Teukolsky equation. We use the code described in [22] (modified with the spectral techniques of [25]) to construct the Newman-Penrose curvature scalar ψ_4. Our code works in the frequency domain, decomposing ψ_4 into $\psi_4 = R^{-1}\sum_{\ell m} Z_{\ell m}\,{}_{-2}Y^{\ell m}(\theta,\phi)\,e^{-im\Omega t}$ where ${}_{-2}Y^{\ell m}(\theta,\phi)$ is a spin-weight -2 spherical harmonic, Ω is the frequency of circular Schwarzschild orbits and R is the distance from the center of mass to the observer. The amplitude $Z_{\ell m}$ is found by first constructing a Green's function to the radial Teukolsky equation, and then integrating that Green's function over a source made from the stress-energy tensor of the small body orbiting the BH; see [22] for specifics.

The radial Teukolsky equation possesses two asymptotic solutions that determine the behavior of ψ_4 at spatial infinity and near the event horizon. In the distant radiation zone, ψ_4 is related to the GWs carried away from the system via $\psi_4 \to 1/2(\ddot{h}_+ - i\ddot{h}_\times)$. Therefore, the solution to the radial Teukolsky equation that describes purely outgoing radiation at spatial infinity can be used to construct the flux of radiation and the waveform that distant observers measure. On the other hand, near the event horizon, ψ_4 describes tidal interactions of the BH with the orbiting body [21]. Thus, the solution to the radial Teukolsky equation that describes purely ingoing radiation at the horizon can be used to construct the radiation flux absorbed by the BH. With these fluxes, we can then calculate the rate at which the orbital radius changes, $\dot{r}$, by noting that for slow backreaction the system evolves through a sequence of geodesic orbits.

We construct the ψ_4 solution on a discrete grid of orbits from $r = 10,000M$ to the Schwarzschild ISCO at $r = 6M$ (in Boyer-Lindquist coordinates), evenly spacing our orbits in $v \equiv \sqrt{M/r}$. (Since stable circular orbits do not exist for $r < 6M$, we cannot infer $\dot{r}$ from dE/dt in this regime.) Errors in the Teukolsky-based waveforms are dominated by truncation of the (ℓ, m) sums in ψ_4 and due to the discretization of the orbital phase space when the fluxes are cubic-spline interpolated from a discrete adiabatic sequence of geodesic orbits. The sums and the discretization are chosen such that the fractional error in the flux is smaller than 10^{-10} [22, 23]. In practice, in the low velocity region $v < 0.1$, we find that the flux is accurate to at least 10^{-13}. Such an error translates to inaccuracies in the GW phase of less than 10^{-2} rads over a 2-year evolution.

Systems, Regions and Models. To demonstrate the flexibility of the EOB model in matching the Teukolsky-based waveforms, we examine two fiducial EMRI systems, labeled system-I and system-II, that sample dif-

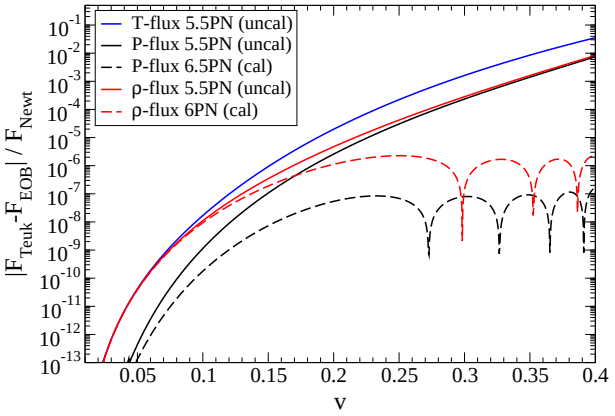

FIG. 1: Absolute value of the difference in the Newtonian normalized Teukolsky and EOB fluxes as a function of orbital velocity. Calibrating the Padé or $\rho-$flux improves the agreement by orders of magnitude

ferent regions of the LISA noise curve. In both cases, we consider a 2-year long quasi-circular inspiral of non-spinning BHs. System-I has $(m_1, m_2) = (10^5, 10)M_\odot$; system-II has $(m_1, m_2) = (10^6, 10)M_\odot$. We do not consider lower or higher total mass binaries as they would either reach the ISCO outside the LISA optimal sensitivity band (LISA's noise rises sharply above $\sim 10^{-2}$ Hz) or lie significantly inside the white-dwarf confusion limit (much below $\sim$ 0.002 Hz [26]). System-II ($m_2/m_1 = 10^{-5}$) begins at an initial separation $r_{\rm in} \simeq 10.6M$ and terminates at the ISCO, sweeping GW frequencies in the range $f_{\rm GW} \in [1.8\times10^{-3}, 4.4\times10^{-3}]$ Hz. System-I ($m_2/m_1 = 10^{-4}$) starts at $r_{\rm in} \simeq 29.34M$ and terminates at $r_{\rm fin} \simeq 16.1M$, sweeping frequencies in the range $f_{\rm GW} \in [4\times10^{-3}, 10^{-2}]$ Hz. The mass ratios we consider, $(10^{-4}, 10^{-5})$ are two orders of magnitude smaller than those studied in the complementary analyses of [9, 10]. As such, our in-band signal is dominated by a long inspiral; the contributions of the final plunge, merger, and ringdown, which dominate the signal of [9, 10], are much less important here. These choices allow the study of the early and late EMRI dynamics, while guaranteeing the GW signal is in the sensitive part of the LISA band.

We define two EOB models differing in the resummation of the radiation-reaction force in Eq. (5). Using the balance law, we write $\widehat{\mathcal{F}}_\Phi = -F/(\nu\Omega)$, where F is the GW energy flux. We use (i) the Padé-approximant to the energy flux [13, 24] $F^{\rm P} = F^p_q(v_{\rm pole})$, where $v_{\rm pole}$ is an adjustable parameter locating the EOB light-ring, and $p+q$ is twice the approximant's PN order [i.e., $(v/c)^{(p+q)}$], and (ii) the ρ-approximant to the energy flux [11] $F^\rho = 2/(16\pi)\sum_{\ell=2}^{\ell=8}\sum_{m=1}^{m=\ell}(m\Omega)^2|Rh_{\ell m}|^2$. Except when investigating the effect of the self-force, the orbital dynamics are computed setting $\nu = 0$ in F, as well as in $A(r)$ and $D(r)$, i.e., for a Schwarzschild BH.

Results. Figure 1 shows the absolute value of the difference between the Newtonian-normalized ($F_{\rm Newt} = 32\nu^2v^{10}/5$) Teukolsky and EOB (*uncalibrated* and *calibrated*) fluxes as a function of the orbital velocity v. The Teukolsky flux includes energy both radiated to infinity and absorbed by the BH's event horizon. The uncalibrated Padé-flux (F^7_4) and ρ-flux are computed through 5.5PN order, but in the Padé flux we also add horizon absorption corrections [27] and set $v_{\rm pole}$ to the Schwarzschild light-ring value. The uncalibrated Taylor-flux (i.e., the PN Taylor-expanded flux [28]) gives a residual about five times worse than the uncalibrated Padé and ρ fluxes. The calibrated Padé-flux (F^7_6) is computed through 6.5PN order, including the horizon absorption corrections, and calibrating $v_{\rm pole}$ and the 6PN and 6.5PN coefficients $\mathcal{F}_{12}$ and $\mathcal{F}_{13}$; see [28] for details. The calibrated ρ-flux is computed through 6PN order, without horizon absorption corrections, and calibrating the 6PN coefficients $c_6^{\rho_{22}}$ in ρ_{22} and the 5PN coefficients $c_5^{\rho_{33}}$ in ρ_{33}; see [11] for details. The calibration is here performed via a least-squares fit to the numerical Teukolsky flux. For velocities $v \in [0.01, 0.1]$ the agreement is better than 10^{-8} with a best agreement of 10^{-13} near $v = 0.01$ for all models.

Comparisons of Teukolsky-based and EOB waveforms are performed once they are aligned in time and phase. Such an alignment guarantees that the fitting factor is maximized over time and phase of coalescence in a matched filtering calculation with white noise [13]. The alignment procedure depends rather sensitively on the alignment window chosen. We choose to align the waveforms in the low-frequency regime, i.e., in the interval $t \in [0, 64]\lambda_{\rm GW}$, where $\lambda_{\rm GW}$ is the GW wavelength, $t \simeq (0, 0.006M)$ $[t \simeq (0, 0.013M)]$ months for system-I [system-II], to a level of 10^{-10} $[10^{-6}]$ rads in the phase for system-I [system-II]. We have checked that choosing any interval window of width $< 2^9\lambda_{\rm GW}$ changes the final dephasing by less than 10^{-3} rads and the relative amplitude difference by less than 10^{-6}.

In the left panel of Fig. 2 we plot the absolute value of the phase difference, or *dephasing*, between the dominant h_{22} mode of the Teukolsky-based and EOB waveforms as a function of time in units of months. We find that after 2-years the dephasing is $\sim$ 40 (3000) rads for system-I (system-II) when using the EOB-model with Taylor-flux (not shown in the figure) [28], a result in qualitative agreement with previous investigations [29]. The EOB model with uncalibrated Padé-flux at 5.5PN has a dephasing of $\sim$ 5 (530) rads for system-I (system-II), which can be reduced to $\sim$ 0.1 (0.01) rads if we employ the calibrated Padé-flux at 6.5PN. The EOB model with uncalibrated ρ-flux at 5.5PN has a dephasing of $\sim$ 10 (530) rads for system-I (system-II), which can be reduced to $\sim$ 2 (0.8) rads if we consider the calibrated ρ-flux at 6PN.

In the right panel of Fig. 2, we compare the amplitude of the dominant mode $A_{22} = |h_{22}|$, computed in the EOB and Teukolsky frameworks. After 2-years of evolution, both the calibrated Padé- and ρ-flux EOB models have a disagreement of $\sim 10^{-5}$ for system-I and $\sim 2\times10^{-3}$ for

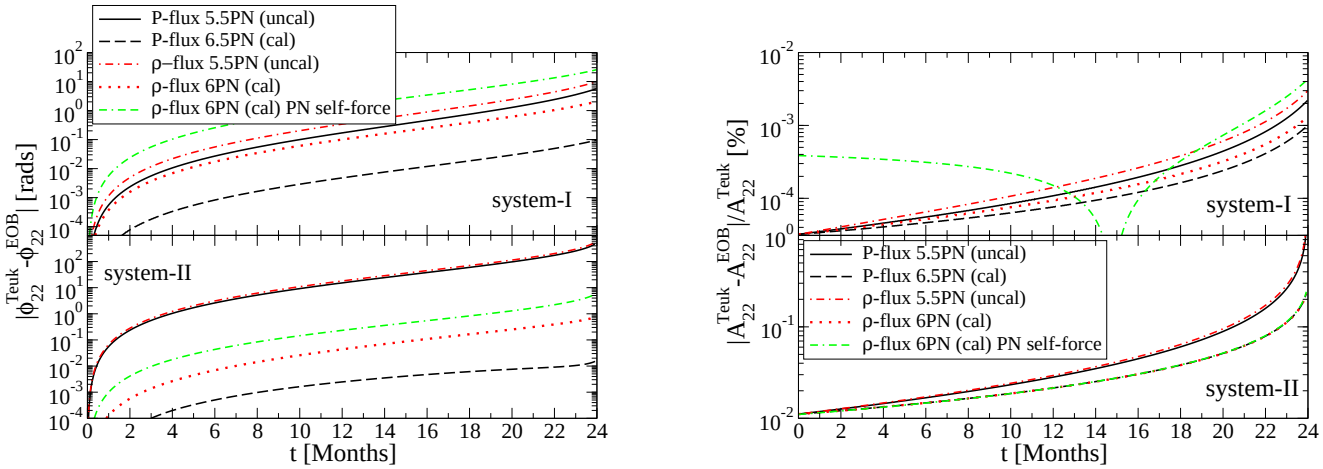

FIG. 2: Absolute value of the dephasing (left) and fractional amplitude difference (right) of the dominant GW $(2,2)$ mode as a function of time in months. Again, with the introduction of calibrated higher-order terms, the differences are small even over a full two year coherent integration.

system-II. Such a phase and amplitude agreement is fantastic when one takes into account the 2-year length of observation, during which the binary of system-I (system-II) evolves over $\sim 2\times10^6$ ($\sim 9\times10^5$) rads. Quite interestingly, we find that if we switch on the relative ν terms in the 3PN EOB Hamiltonian Eq. (1) (conservative self-force) and in the flux (dissipative self-force[1]) the dephasing, for the EOB-model with ρ-flux at 6PN, increases to ~ 27 (6) rads for system-I (system-II), while the Newtonian normalized amplitude difference increases to 4×10^{-4} (2.5×10^{-3}) for system-I (system-II). We notice that the main effect comes from the dissipative self-force, a result consistent with [30] for circular orbits (see e.g. [31–33] for more details on the PN self-force).

We also compare the strongest higher harmonics using the EOB model with Padé-flux at 6.5PN. In the case of the $(\ell,m)=(3,3)$ and $(\ell,m)=(4,4)$ modes we find dephasings of ~ 0.14 (0.07) and ~ 0.18 (0.09) rads, and normalized amplitude differences of $\sim 6\times10^{-5}$ (4×10^{-3}) and $\sim 3\times10^{-4}$ (9×10^{-3}), for system-I (system-II). These dephasings are comparable to those found for the $(\ell,m)=(2,2)$ mode because in both frameworks the GW phase (and frequency) can be computed directly from the orbital phase (and frequency), up to errors of less than ~ 1 rad over a 2-year integration. As a consequence, the above comparisons are almost entirely governed by the trajectories of the test particle. Finally, we find that higher harmonics contribute significantly less to the signal-to-noise ratio relative to the $(2,2)$ mode. In particular, we computed the signal-to-noise ratio averaged over beam-pattern functions with a noise spectral density that includes white-dwarf confusion noise. Including up to $\ell=5$ ($\ell=7$) for system-I (system-II) guarantees a recovery of 97% of the total signal-to-noise ratio, with the $\ell=m$ modes the most dominant.

Data Analysis Implications and Discussion. The above results have demonstrated that the EOB framework can be used to model EMRIs for LISA data analysis purposes, with the advantage of allowing for the consistent inclusion of both dissipative and conservative PN self-force terms. In addition, such terms allow the construction of waveforms from intermediate-mass ratio inspirals, where first-order BH perturbation theory is expected to fail. The comparisons made here, however, serve only as a proof-of-principle, as one must now generalize the formalism to more generic spinning EMRIs, and more complicated orbital geometries.

The EOB framework also allows us to provide, for the first time, a metric-based estimate of the number of templates needed for EMRI systems in LISA data analysis [24, 34]. As a coherent 2-year integration in the search of EMRIs is computationally prohibitive, a hierarchical search that collects power from coherent searches of shorter segments was proposed in [1]. The maximum segment length set by computational limits in such a hierarchical search is estimated to be less than 2 months. For a 2-month evolution, we estimate that one requires less than 10^7 EOB templates to cover the template bank with a minimal match of 0.97 in the total mass range $(10^5$–$10^6)M_\odot$ and mass ratio range $(10^{-4}$–$10^{-5})$.

Acknowledgments. We are grateful to F. Pretorius and E. Poisson for comments and to W. Throwe for computational assistance. NY, AB and YP, and SAH acknowledge support from the NSF grants PHY-0745779, PHY-0603762, PHY-0903631, and PHY-0449884; AB, SAH and MCM also acknowledge support from NASA grants NNX09AI81G, NNX08AL42G and NNX08AH29G.

[1] Sometimes *all* of the energy loss due to radiation, is considered part of the dissipative force (even the $\nu=0$ part), but here we refer only to the ν-dependent terms in the flux.

[1] J. R. Gair, L. Barack, T. Creighton, C. Cutler, S. L. Larson, E. S. Phinney, and M. Vallisneri, Classical and Quantum Gravity **21**, 1595 (2004).
[2] S. A. Hughes, AIP Conf. Proc. **873**, 233 (2006).
[3] A. Buonanno and T. Damour, Phys. Rev. **D59**, 084006 (1999).
[4] A. Buonanno and T. Damour, Phys. Rev. **D62**, 064015 (2000).
[5] T. Damour, P. Jaranowski, and G. Schaefer, Phys. Rev. **D62**, 084011 (2000).
[6] T. Damour, Phys. Rev. **D64**, 124013 (2001).
[7] A. Buonanno, Y. Chen, and T. Damour, Phys. Rev. **D74**, 104005 (2006).
[8] T. Damour, P. Jaranowski, and G. Schaefer, Phys. Rev. **D77**, 064032 (2008), 0711.1048.
[9] A. Nagar, T. Damour, and A. Tartaglia, Class. Quant. Grav. **24**, S109 (2007).
[10] T. Damour and A. Nagar, Phys. Rev. **D76**, 064028 (2007).
[11] T. Damour, B. R. Iyer, and A. Nagar, Phys. Rev. **D79**, 064004 (2009).
[12] T. Damour and A. Nagar, Phys. Rev. **D79**, 081503 (2009).
[13] A. Buonanno et al., Phys. Rev. **D79**, 124028 (2009).
[14] P. Amaro-Seoane et al., Class. Quantum Grav. **24**, 113 (2007).
[15] M. C. Miller et al., ApJ Letters **631**, L117 (2005).
[16] D. Syer, C. J. Clarke, and M. J. Rees, Mon. Not. R. Astron. Soc. **250**, 505 (1991).
[17] Y. Levin (2003), astro-ph/0307084.
[18] Y. Levin, Mon. Not. Roy. Astron. Soc. **374**, 515 (2007).
[19] J. Wang and D. Merritt, ApJ **600**, 149 (2004).
[20] S. A. Teukolsky, Phys. Rev. Lett. **29**, 1114 (1972).
[21] S. A. Teukolsky, Astrophys. J. **185**, 635 (1973).
[22] S. A. Hughes, Phys. Rev. **D61**, 084004 (2000).
[23] S. A. Hughes, Phys. Rev. **D64**, 064004 (2001).
[24] T. Damour, B. R. Iyer, and B. S. Sathyaprakash, Phys. Rev. **D57**, 885 (1998).
[25] R. Fujita and H. Tagoshi, Prog. Theor. Phys. **113**, 1165 (2005).
[26] A. J. Farmer and E. S. Phinney, Mon. Not. Roy. Astron. Soc. **346**, 1197 (2003).
[27] Y. Mino et al., Prog. Theor. Phys. Suppl. **128**, 1 (1997).
[28] M. Boyle et al., Phys. Rev. **D78**, 104020 (2008).
[29] I. Mandel and J. R. Gair, Class. Quant. Grav. **26**, 094036 (2009).
[30] A. Pound and E. Poisson, Phys. Rev. **D77**, 044013 (2008).
[31] L. Blanchet, S. Detweiler, A. L. Tiec, and B. F. Whiting (2009), 0910.0207.
[32] L. Barack and N. Sago, Phys. Rev. Lett. **102**, 191101 (2009).
[33] T. Damour (2009), 0910.5533.
[34] B. J. Owen, Phys. Rev. **D53**, 6749 (1996).